Progress In Electromagnetics Research C, Vol. 173, 103–115, 2025

PIER C

(Received 12 May 2026, Accepted 17 August 2026, Scheduled 2 September 2026)

Bistatic Radar for Multi-Target Detection Using Microstrip Patch Antennas

Ankita Malhotra[1], Priyal Veera[2,*], Aryan Bhalkar[2], Rajiv Datta[2], Shubham Tayade[2], and Amit A. Deshmukh[2]

[1]*Auckland University of Technology, Auckland, New Zealand*
[2]*EXTC Department, SVKM's Dwarkadas J. Sanghvi College of Engineering, Mumbai, India*

ABSTRACT: This paper presents a compact, low-cost, frequency-domain bistatic radar system using two identical square microstrip patch antennas fabricated on an FR-4 substrate ($\varepsilon_r = 4.4$, thickness $= 1.6$ mm). The antenna incorporates a suspended air-gap configuration to enhance bandwidth and radiation efficiency, and is designed to resonate near 3.3 GHz. The antenna was designed and optimised using CST Microwave Studio and experimentally validated using a Vector Network Analyser (VNA). Simulation results demonstrate a peak gain of 6.6 dBi and radiation efficiency of 83.2%. The fabricated antenna exhibits a measured peak gain of 7.0 dBi at 3.23 GHz and a $|S_{11}| \leq -10$ dB bandwidth from approximately 3.0 to 3.5 GHz, with a measured resonance minimum of -14.3 dB at 3.27 GHz. The bistatic radar system operates over a swept frequency range of 2.8 to 3.8 GHz, acquiring complex S_{21} parameters at each discrete frequency step. The received S_{21} data is processed using background subtraction to suppress antenna coupling and background clutter, followed by an Inverse Fast Fourier Transform (IFFT) for range-domain target localisation. The proposed system is experimentally validated in single-target and multiple-target scenarios. Closely spaced targets are further characterised using a CLEAN iterative deconvolution algorithm as a post-processing step. Consistent target localisation across all scenarios is confirmed by two-dimensional radar images obtained from cross-range scanning. The results demonstrate the feasibility of a low-cost bistatic radar platform for short-range sensing applications including security scanning, remote target localisation, and multi-target detection.

1. INTRODUCTION

The rapid advancement of microwave sensing technologies has established radar as a key technology for object detection, localisation, and imaging across a wide range of applications, including through-wall detection, ground-penetrating radar (GPR), vital sign monitoring, and multi-target localisation [1–9]. The growing demand for economical and compact systems capable of resolving multiple targets in cluttered, short-range environments has driven significant advances in radar architectures, with an emphasis on reducing hardware complexity while maintaining reliable sensing performance [2, 5].

Among short-range sensing approaches, frequency-domain radar systems using a Vector Network Analyser (VNA) have gained recognition for their simple hardware architecture, compact printed-circuit implementations, and high dynamic range. In this approach, the VNA sweeps a discrete set of frequencies and acquires the complex S-parameter response at each frequency step, which is subsequently transformed to the time domain using an Inverse Fast Fourier Transform (IFFT) to obtain range-domain target information [7, 14]. The range resolution of such a system is defined by $\Delta R = c/2B$, where c is the speed of light, and B is the total swept bandwidth, while the maximum unambiguous range is inversely proportional to the frequency step size. For compact and cost-effective implementations, microstrip patch antennas fabricated on a standard FR-4 substrate ($\varepsilon_r \approx 4.4$) provide a practical front-end solution, offering realised gains of approximately 4–7 dB and $|S_{11}| \leq -10$ dB impedance bandwidth suitable for short-range radar applications [12, 13]. Existing work has explored frequency-domain radar systems across diverse hardware configurations. Kozlov et al. [3] demonstrated stepped-frequency signal processing with inter-period subtraction for stationary human detection through walls. Acar et al. [2] presented an S-band zero-IF Stepped-Frequency Continuous Wave (SFCW) radar employing a uniform linear array for simultaneous through-wall range, respiration-rate, and direction-of-arrival estimation. Jia et al. [7] proposed a dual-station SFCW radar exploiting cross-correlation for locating multiple stationary human targets. For radar imaging applications, ultra-wideband antenna structures, such as miniaturised Vivaldi arrays, are widely employed because of their broad impedance bandwidth and directive radiation characteristics, although these designs generally incur higher fabrication cost and hardware complexity than conventional microstrip patch antennas [6, 8, 9]. To suppress antenna coupling and environmental clutter in static measurement environments, background subtraction remains one of the most widely adopted signal-processing techniques [4, 6, 15]. Resolving closely spaced targets within a single IFFT range bin, however, remains challenging because reflections from nearby scatterers overlap in the time domain. To address this limitation, iterative deconvolution techniques such as the CLEAN algorithm have been employed to improve target separabil-

* Corresponding author: Priyal Veera (piyuveera59@gmail.com).

doi:10.2528/PIERC26051202

Published by THE ELECTROMAGNETIC ACADEMY

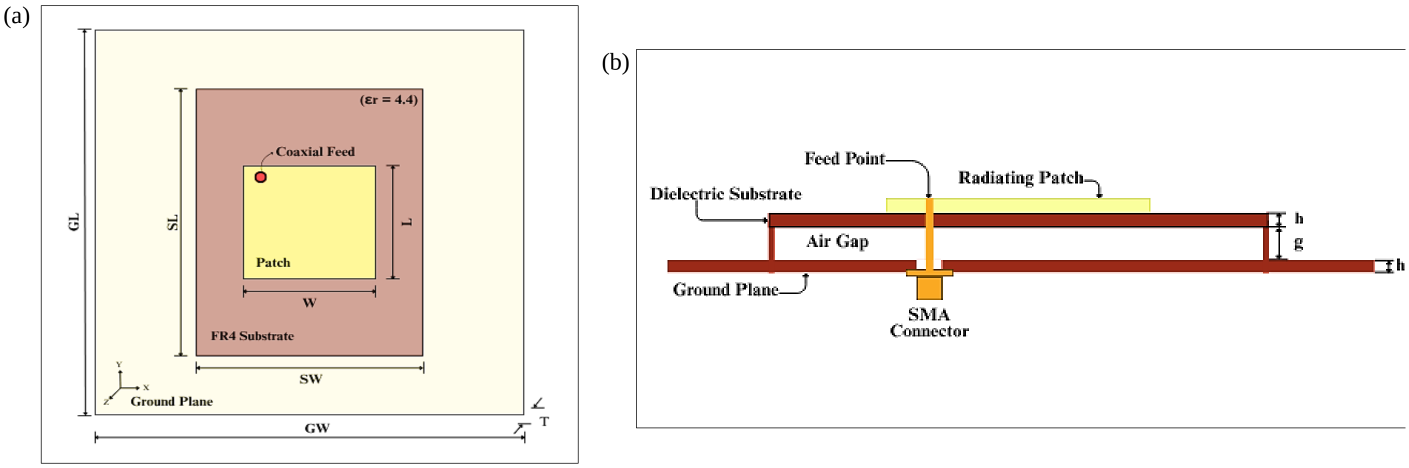

FIGURE 1. Geometry of the square microstrip patch antenna. (a) Top view and (b) cross-sectional view.

ity beyond the hardware range-resolution limit [16–19]. Two-dimensional radar images generated from cross-range scanning have been widely used to validate localisation accuracy and visualise target distributions in short-range radar systems [6, 7]. Despite advances in clutter suppression, multi-target detection, and two-dimensional radar imaging, there remains a lack of compact bistatic radar systems experimentally validated across all three capabilities within a single low-cost platform. Most existing systems rely on ultra-wideband antenna arrays, specialised substrates, multi-element architectures, or dedicated radar hardware, thereby increasing implementation complexity and fabrication cost [2, 6, 9–11]. A detailed comparison of the proposed system with these reported works is presented in Table 4. This work addresses the identified gap by proposing a compact bistatic radar system implemented on a standard FR-4 substrate using two identical suspended-substrate microstrip patch antennas. A signal-processing pipeline comprising background subtraction, IFFT-based range profiling, and CLEAN iterative deconvolution is implemented and experimentally validated for reliable single-, two-, and three-target detection in a short-range free-space environment.

2. SYSTEM DESIGN AND METHODOLOGY

2.1. Antenna Design

A square microstrip patch antenna is fabricated on an FR-4 dielectric substrate ($\varepsilon_r = 4.4$, thickness $= 1.6$ mm) referenced with a contiguous copper ground plane. It is fed via a coaxial probe feed. To enhance bandwidth and radiation efficiency, an air gap is implemented between the radiating patch and the ground plane. The antenna geometry is shown in Figures 1(a) and (b), and all optimised antenna dimensions are summarised in Table 1. The proposed antenna, owing to its compact planar form factor and the use of standard FR-4 substrate, is suitable for low-cost bistatic radar front-ends. The total antenna assembly with thickness $T = 4.0$ mm comprises an upper FR-4 substrate ($h_1 = 1.6$ mm), air gap ($g = 0.8$ mm) and a lower FR-4 ground plane ($h_2 = 1.6$ mm), with the remainder accounted for by copper cladding on both boards.

TABLE 1. Optimized dimensions of the proposed antenna.

Parameters	Symbols	Value (mm)
Length of the substrate	SL	65
Width of the substrate	SW	57
Length of the Patch	L	29
Width of the Patch	W	31
Length of the Ground Plane	LG	102
Width of the Ground Plane	WG	108
Total Antenna Assembly Thickness	T	4.0
Height of dielectric substrate (each layer)	h	1.6
Air gap between patch and ground plane	g	0.8

2.2. Antenna Characterisation

By using a two-port VNA, the fabricated antenna's performance was verified. Comparison of simulated and measured $|S_{11}|$ responses is depicted in Figure 2, where the simulation predicted a resonance minimum of -17.1 dB at 3.32 GHz while the measured resonance minimum is -14.3 dB at 3.27 GHz, with a $|S_{11}| \le -10$ dB spanning approximately 3.0 to 3.5 GHz. The small downward shift in resonant frequency is consistent with suspended-substrate behaviour: the air-gap-coupled feed modifies the fringing field distribution and slightly alters the effective boundary conditions. The resulting shift, at under 2% of the simulated value, falls within acceptable fabrication tolerance for FR-4 prototypes.

The three-layer dielectric stack FR-4 ($h_1 = 1.6$ mm, $\varepsilon_1 = 4.4$), air gap ($g = 0.8$ mm, $\varepsilon_{air} = 1.0$), and FR-4 ($h_2 = 1.6$ mm, $\varepsilon_2 = 4.4$) acts as a series capacitor combination, yielding an effective dielectric constant lower than the nominal FR-4 value. Using the series capacitor approximation:

$$\varepsilon_{\mathit{eff}} = \frac{h_{total}}{\frac{h_1}{\varepsilon_1} + \frac{g}{\varepsilon_{air}} + \frac{h_2}{\varepsilon_2}} = \frac{4.0}{0.364 + 0.800 + 0.364} = 2.62 \quad (1)$$

Substituting $\varepsilon_{\mathit{eff}} = 2.62$ into $f_r = c/(2L\sqrt{\varepsilon_{\mathit{eff}}})$ with $L = 29$ mm gives an estimated resonance near 3.20 GHz, in reason-

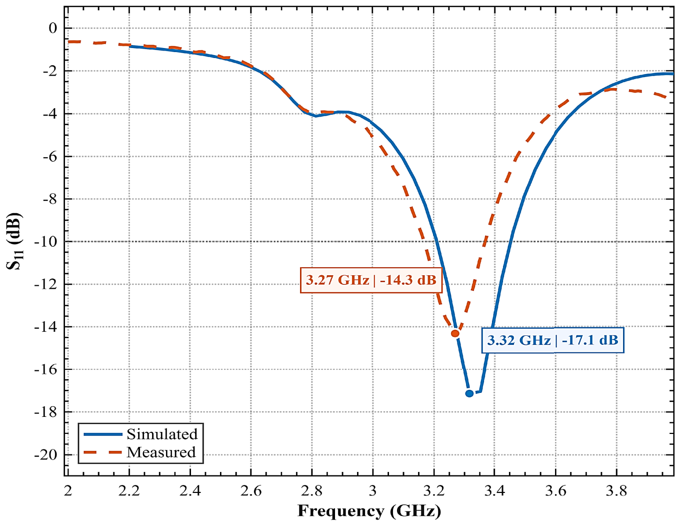

FIGURE 2. Simulated vs. measured S_{11}.

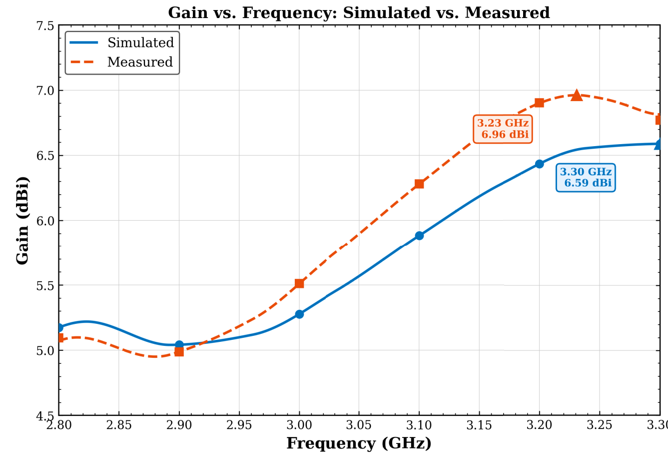

FIGURE 3. Simulated vs. measured gain.

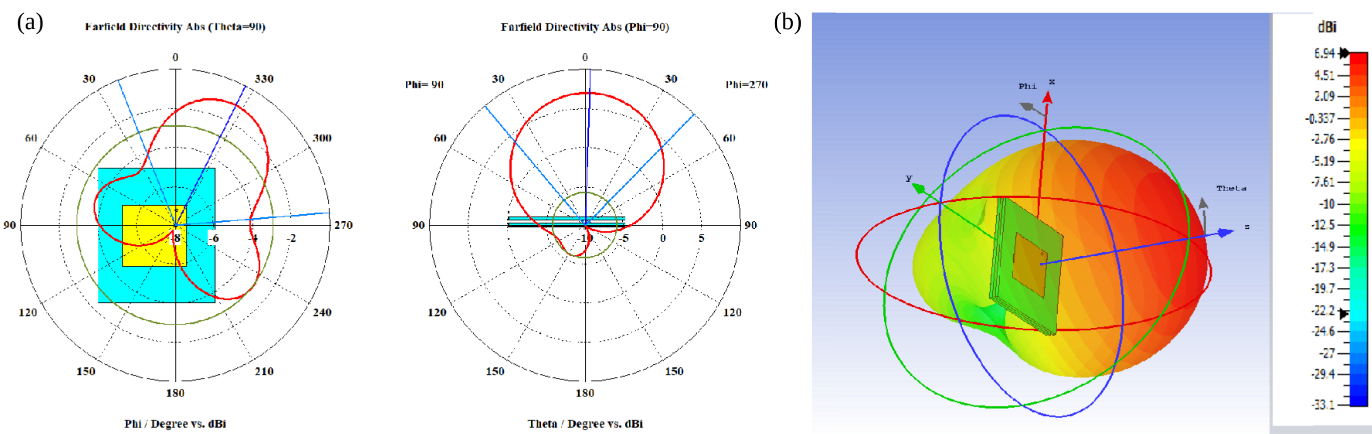

FIGURE 4. (a) Far-field radiation pattern (E- and H-plane) at 3.32 GHz and (b) 3D Far-field radiation pattern of the antenna.

able agreement with the measured value stated above. The remaining difference is attributed to the extended ground plane ($LG = 102$ mm, $WG = 108$ mm), which slightly raises the effective resonant frequency by modifying the distributed fringing capacitance. Simulated and measured antenna gains as a function of frequency are presented in Figure 3. The simulated peak gain is 6.6 dBi. The Friis transmission equation was applied to derive the measured gain for bistatic measurements with the identical antenna pair separated by 4.2 m at a transmitted power of 10 dBm. Since both antennas are identical ($G_t = G_r = G$), the Friis transmission equation gives:

$$G\,[\text{dBi}] = \frac{P_r\,[d\text{Bm}] - P_t\,[\text{dBm}] + \text{FSPL}\,[\text{dB}]}{2} \tag{2}$$

where $\text{FSPL} = 20\log_{10}\frac{4\pi d}{\lambda}$ is the free-space path loss at separation d; P_r is the measured received power; and $P_t = 10$ dBm is the transmitted power. At 4.2 m, the antennas are well into the far-field region (far-field distance $2D^2\lambda \approx 0.09$ m at 3.3 GHz). Applying Equation (2) yields a peak extracted gain of 7.0 dBi at 3.23 GHz, deviating by only 0.4 dBi from simulation, validating the antenna design. Figure 4(a) demonstrates the 2D directivity patterns for the E-plane ($\varphi = 90°$) and H-plane ($\theta = 90°$). The simulated 3D far-field radiation pattern at 3.32 GHz is shown in Figure 4(b). The principal plane cross-sections of the 3D pattern, shown in Figure 4(a), provide clearer resolution of the lobe structure and confirm the broadside characteristic. Typical of the TM_{10} resonance mode, the antenna exhibits a broadside radiation characteristic with a maximum gain of 6.6 dBi directed normal to the patch ($\theta = 0°$). The antenna's predominant radiation above the ground plane supports its suitability for bistatic radar applications. Both planes demonstrate a symmetric, squint-free broadside characteristic centred at ($\theta = 0°$).

Back-lobe levels are effectively suppressed, due to the extended ground plane, which minimises radiation into the lower hemisphere. This symmetric profile ensures both transmitter and receiver maintain a consistent beam toward the target throughout cross-range scanning. Figure 5(a) shows the simulated surface current distribution at 3.32 GHz. A half-sinusoidal variation along the patch length confirms the fundamental TM_{10} resonant mode, with current concentrated along the non-radiating edges and a symmetric distribution about the

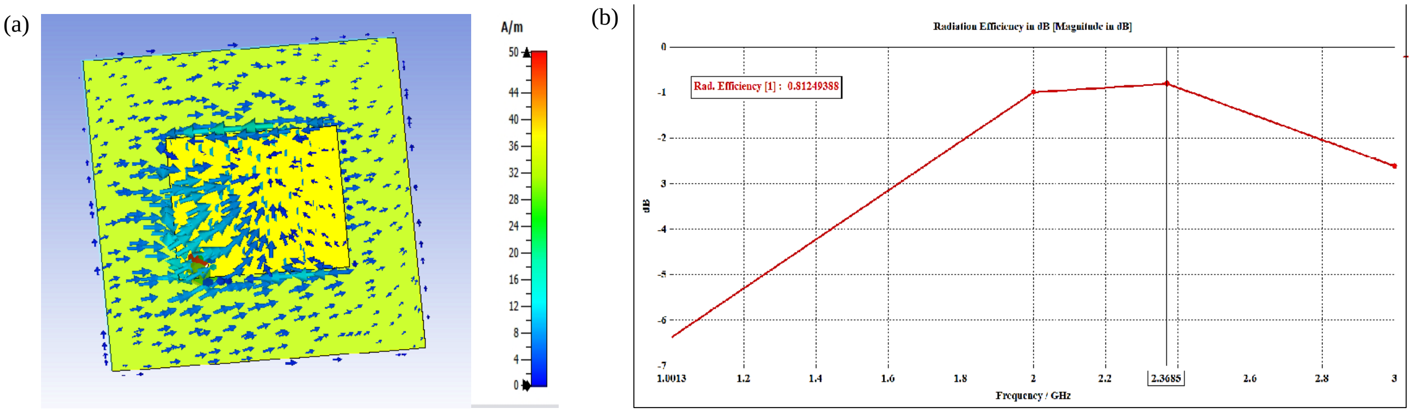

FIGURE 5. (a) Surface current distribution of the antenna and (b) radiation efficiency.

centreline. Figure 5(b) shows the radiation efficiency, with a peak value of 83.2%. This is a significant result for a lossy FR-4 substrate ($\tan\delta \approx 0.02$), achieved primarily through the reduced effective dielectric loading of the suspended air-gap configuration.

2.3. Radar Measurement Setup

The bistatic radar measurement system consists of two identical fabricated microstrip patch antennas acting as transmitter and receiver, respectively, connected to two ports of the VNA via low-loss SMA coaxial cables. A fixed bistatic baseline separation of 5 cm is maintained throughout all experiments. The VNA sweeps from 2.8 to 3.8 GHz across 201 equally spaced frequency points, acquiring the complex S_{21} parameter (magnitude and phase) at each step. The 1 GHz swept bandwidth provides a theoretical range resolution of $\Delta R = c/2B = 0.15$ m. The maximum unambiguous range, given by $R_{\text{max}} = c/(2\Delta f)$ with $\Delta f = 5$ MHz, is 30 m, well beyond the short-range measurement scenarios considered here.

The antennas are positioned facing the target region with the fixed bistatic baseline maintained throughout all experiments. At each cross-range position, two datasets were collected: one without any target present (background reference) and one with the targets at their designated positions. Cross-range scanning was performed by laterally shifting targets to discrete positions. The measurements were conducted in a laboratory environment where multipath reflections from the table surface and surrounding structures contribute to the received signal alongside target echoes. Background subtraction mitigates stationary multipath under the assumption that environmental reflections remain stable between reference and target measurements. The consistency of detected peak positions across repeated cross-range scan positions confirms that residual multipath effects did not cause false detections or range errors in the present setup. Single-target experiments used five standoff distances along the boresight axis: 0.36 m, 0.41 m, 0.53 m, 0.61 m, and 0.84 m. In this notation, C denotes the centre position at 0 cm lateral displacement; L denotes positions to the left (negative cross-range direction); and R denotes positions to the right (positive cross-range direction), with the numeral indicating the step count at

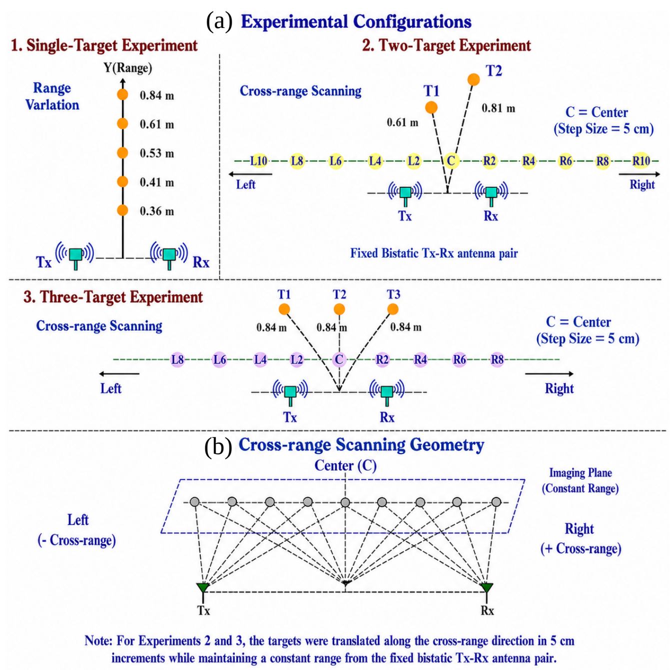

FIGURE 6. (a) Experimental configurations for single-target, two-target, and three-target experiments, and (b) cross-range scanning geometry.

5 cm intervals from the centre. The full experimental geometry is illustrated in Figure 6.

2.4. Signal Processing Pipeline

The signal processing approach follows a background-subtraction method implemented in MATLAB. Since the received S_{21} data contains direct antenna coupling, environmental reflections, and target-masked echoes, background removal is performed before range profiling. The background-subtracted differential spectrum is expressed as:

$$S_{diff(f)} = S_{target(f)} - S_{ref(f)} \tag{3}$$

where $S_{target(f)}$ represents the received signal with the target present; $S_{diff(f)}$ represents the background-subtracted signal; and $S_{ref(f)}$ represents the reference signal without a target. Both spectra are reconstructed as complex quantities from the

TABLE 2. Summary of experimental configurations.

Parameter	Single-target	Two-target	Three-target
No. of targets	1	2	3
Target range(s)	0.36–0.84 m	T1: 0.61 m, T2: 0.81 m	0.84 m (all)
Cross-range positions	5 boresight standoffs	11 (L10-R10, 5 cm steps)	9 (L8-R8, 5 cm steps)
Target lateral separation	N/A	Off-boresight	T1: 9.5 cm, T3: 7 cm from T2
Total lateral span	N/A	N/A	16.5 cm

recorded magnitude (dB) and phase (degrees) as:

$$S(f) = 10^{\frac{(|S_{21}|_{\text{dB}})}{20}} e^{(j\phi_{rad})} \tag{4}$$

The background-subtracted spectrum $S_{diff(f)}$ is then transformed to the time domain using a zero-padded IFFT, providing interpolated range profiles for target localisation:

$$s(t) = F^{-1}\{S_{diff(f)})\} \tag{5}$$

Zero-padding improves range-axis interpolation for locating peaks but does not improve the fundamental range resolution ($\Delta R = 15$ cm, established in Section 2.3).

3. RESULTS

This section presents experimental results across three target configurations. In each case, the background subtraction and IFFT pipeline in Section 2.4 is applied uniformly. Table 2 summarizes experimental configurations of single-, two-, and three-target experiments.

3.1. Single-Target Detection

To demonstrate the efficacy of the proposed bistatic radar setup, single-target detection forms the baseline evaluation experiment. Figure 7 shows the experimental setup for single target detection. In this experiment, a single metallic target was placed in the antenna's field of view at different standoff distances along the boresight axis: 0.356 m, 0.406 m, 0.533 m, 0.610 m, and 0.838 m, respectively. At each scan position, a full S_{21} sweep was acquired and processed by applying the IFFT and background-subtraction pipeline to obtain the time-domain range profiles. Figure 8 shows the system's time-domain response at a distance $d = 0.533$ m. In this case, the waveform demonstrates a dominant peak followed by oscillations, which are sidelobe artefacts from the rectangular spectral window obtained during signal processing and IFFT operation. The dominant peak in waveforms corresponds to the two-way propagation delay of the target reflection and is used for primary range estimation. The waveforms are presented in linear amplitude to clearly emphasise the dominant peak relative to sidelobe structure for range estimation.

To independently verify peak positions, the time-domain propagation delay of the target reflection is calculated using the following radar range equation:

$$\Delta t = \frac{(2 \times R)}{v_p} \tag{6}$$

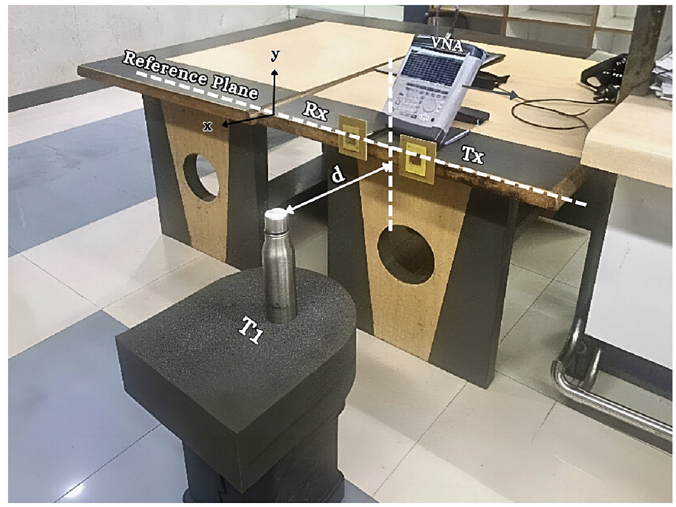

FIGURE 7. Experimental setup for single-target detection.

where R is the physical standoff distance between antennas and the target, and $v_p = 3 \times 10^8$ m/s is the free-space propagation velocity. The detected range is recovered from the observed peak time t_{peak} as:

$$R_{detected} = \frac{(v_p \times t)}{2} \tag{7}$$

For the 0.53 m case, Equation (6) gives $\Delta t = 2 \times 0.53/(3 \times 10^8) = 3.55$ ns. The detected peak at $t_{peak} = 3.63$ ns yields $R_{detected} = (3 \times 10^8 \times 3.63 \times 10^{-9})/2 = 0.544$ m, a range error of $|0.53 - 0.544| = 0.01$ m, well within the 15 cm range resolution.

Table 3 summarises results for all five target positions. The maximum error of 0.09 m occurred at the closest standoff distance due to partial overlap with antenna coupling clutter. All measured errors remained within the theoretical range resolution (15 cm), confirming reliable localisation. The background-subtracted range profiles from all 5 target cases were assembled individually to create a matrix, and then, a two-dimensional heatmap was generated to visualise the system's spatial detection capability. Figure 9 presents the resulting combined heatmap, with target distance from the antenna on the vertical axis and detected range on the horizontal axis, consolidating all five standoff positions into a single plot.

The heatmap exhibits five distinct bright clusters, each corresponding to one target standoff distance and confirming con-

TABLE 3. Manual range validation.

Target Distance (m)	Expected Peak (ns)	Detected Peak (ns)	Detected Range (m)	Error (m)
0.36	2.37	2.97	0.45	0.09
0.41	2.71	3.24	0.49	0.08
0.53	3.55	3.63	0.54	0.01
0.61	4.06	4.49	0.67	0.06
0.84	5.59	5.78	0.87	0.03

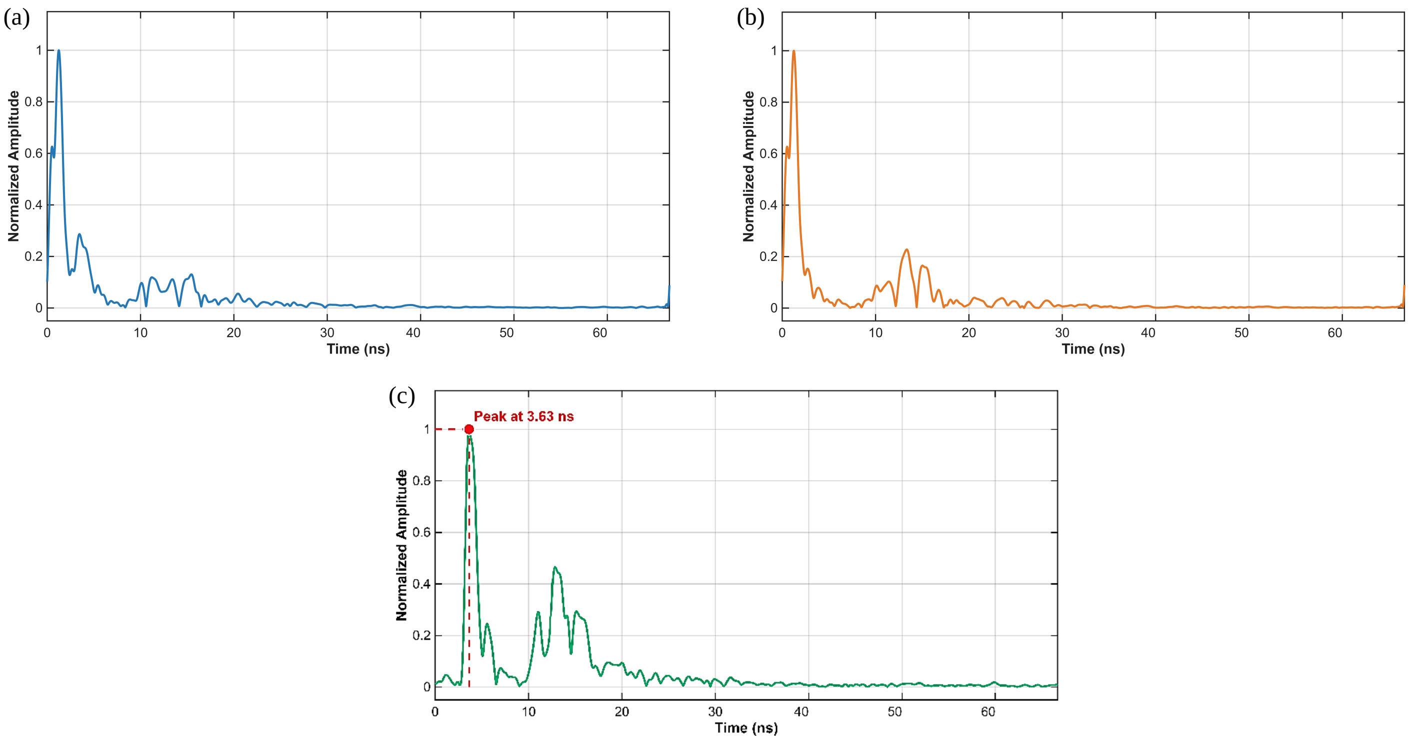

FIGURE 8. Range profiles for one-target at 0.53 m. (a) Target-present response at centre position, (b) without target response (background reference), and (c) background-subtracted range profile.

sistent detection at each position. Progressing from the bottom (0.36 m) to the top (0.84 m) of the plot, the bright cluster shifts monotonically toward larger detected range, tracking the expected 2.4 : 1 distance ratio between the closest and furthest positions. Good spatial agreement between the expected and detected target ranges at each distance is indicated by the white × (expected) and + (detected) markers overlaid on the ideal locus. The detected ranges remain within the expected range-resolution limits, indicating no systematic range bias over the measurement window. Corresponding to free-space path-loss behaviour, the amplitude of detected peaks decreases progressively as target distance increases, consistent with the bistatic radar equation where $P_r \propto 1/(R_{tx} \cdot R_{rx})^2$. For the near-collinear geometry with a 5 cm bistatic baseline, $R_{tx} \approx R_{rx} \approx R$, and received power scales approximately as $P_r \propto 1/R^4$. The closest standoff distance (0.36 m) exhibits slightly elevated amplitude due to residual antenna-coupling clutter, whereas beyond this near-range region, the peak amplitude decreases monotonically with distance, indicating physically consistent propagation behaviour.

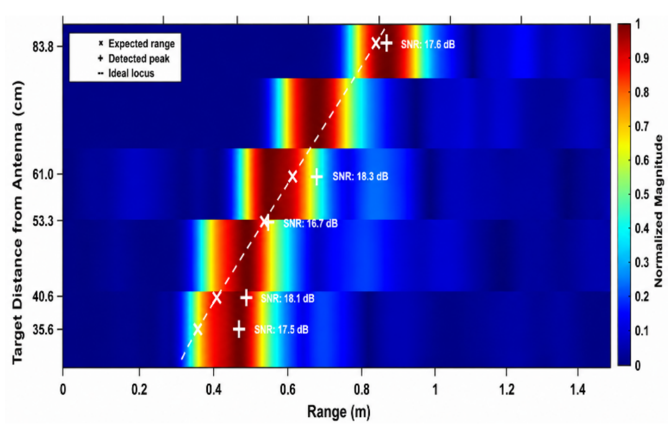

FIGURE 9. 2D heatmap for single-target detection across all five standoff distances (0.36–0.84 m).

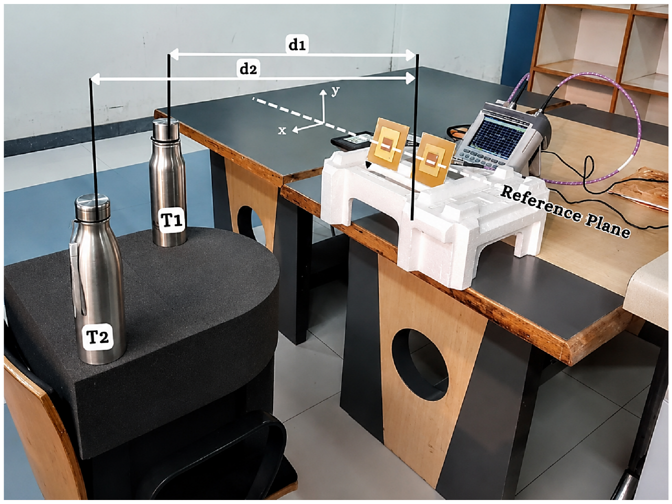

FIGURE 10. Experimental setup for two-target detection.

3.2. Two-Target Detection

Two-target experiments evaluate the system's capability to detect multiple targets in a single measurement. Figure 10 represents the experimental setup for the two-target experiment. Unlike the single-target case, two targets differ in range and are not co-located on the boresight axis, adding complexity. The first target (T1) was placed along the boresight axis at $d_1 = 0.61$ m from the transmitting antenna. The second target (T2) was placed diagonally off the boresight from the transmitting antenna at $d_2 = 0.81$ m. This placement was intentional to evaluate if the system can detect a target that is not directly in the specular reflection path of the antenna boresight. Cross-range scanning covered 11 positions (L_{10} through R_{10}, 5 cm steps; see Table 2 and Figure 6 for exact offsets). Figure 11 represents three waveforms at (Centre, 0 cm cross-range offset): target-present, background result, and subtracted response. Both the target-present and background results are dominated by large peaks at $t \approx 1$–2 ns, which is due to antenna coupling and near-field clutter common to both measurements. After subtraction, the antenna-coupling and near-field clutter common to both measurements were effectively reduced, producing a clearer target-induced reflection. Using Equation (7), the dominant peak observed at $t = 4.06$ ns corresponds to a detected range of 0.61 m. This is accurate in the physical placement of the first target (T1). The range error between expected and detected positions is 0.001 m, confirming high localisation accuracy. Similarly, the second dominant peak corresponding to target 2 (T2) is detected at $t = 5.44$ ns.

The detected range corresponds to approximately 0.81 m, with a range error of 0.006 m, confirming reliable detection of the second target although it is placed diagonally off the antenna's boresight axis. The observed amplitude difference between T1 and T2 is physically expected despite both being identical metallic targets. The bistatic received power scales as $P_r \propto 1/(R_{tx} \cdot R_{rx})^2$, where R_{tx} and R_{rx} are transmitter-to-target and target-to-receiver distances, respectively. For T1 at 0.61 m on boresight, $R_{tx} \cdot R_{rx} \approx 0.37\,\text{m}^2$, while for T2 at 0.81 m, $R_{tx} \cdot R_{rx} \approx 0.66\,\text{m}^2$, corresponding to approximately 5 dB greater path loss. Additionally, T2's lateral offset from the boresight axis places it at a non-zero off-axis angle, reducing the effective two-way antenna gain relative to T1. The combination of greater path loss and reduced off-axis antenna gain accounts for the weaker and spatially spread response of T2 observed in both the waveform and the heatmap. These observations demonstrate that the bistatic radar system shows reliable multi-target detection across all lateral scanning positions. Figure 11(d) presents the two-dimensional heatmap, assembled using subtracted range profiles of 11 cross-range positions. White plus (+) markers indicate the detected range of T1, and white cross (×) markers indicate the detected range of T2 at each cross-range position.

The heatmap depicts a strong, spatially consistent bright intensity region at $R \approx 0.6$ m, which is closely aligned to T1 placed at 0.61 m. A second region of moderate intensity is observed at 0.81–0.86 m, corresponding to T2 placed at 0.81 m. Compared to T1, the T2 response appears weaker and partially scattered across all cross-range scanning positions. Although this leads to a reduced signal-to-noise ratio, detecting a secondary reflection region confirms the system's ability to successfully detect target 2 (T2). The generated heatmap validates the proposed system's capability to detect multiple spatially separated targets simultaneously, including targets placed outside the antenna boresight axis.

3.3. Three Target Detection

The three-target experiment consisted of three metallic objects along a common transverse plane. Figure 12 represents the experimental setup for the three-target experiment. All three targets were placed at an equal range of 0.838 m from the transmitting antenna, separated only in the lateral cross-range dimension (Table 2): centre target T2 on boresight, T3 displaced 7 cm to the right, and T1 displaced 9.5 cm to the left, for a total lateral span of 16.5 cm. Cross-range scanning covered 9 positions (L8 through R8, 5 cm steps).

Because all three targets share nearly the same range, their echoes arrive at almost identical time delays and occupy the same range bin after IFFT processing. Consequently, their responses overlap and produce a single merged peak. This outcome is physically expected and does not indicate a system fault. The corresponding bandwidth requirement for closely spaced targets in range, $B_{\text{min}} = c/(2 \times R_{\text{min}}) = 3 \times 10^8/(2 \times 0.07) \approx 2.14$ GHz. Even though a bandwidth of ~ 2.14 GHz would be required, it is important to note that increasing the bandwidth alone would not help resolve the targets, since targets are co-located in range. Angular resolution through antenna arrays or synthetic aperture radar (SAR) processing would be required.

Figure 13 shows the waveform at the centre scanning position. As in the two-target case (Section 3.2), antenna-coupling peaks at $t \approx 1$–2 ns are suppressed by background subtraction, revealing the target reflection. After subtraction, the dominant peak is observed at $t = 5.42$ ns, corresponding to a detected range of 0.81 m using Equation (7). This range corresponds to the physical placement of T2 located at the centre position of the experiment setup. Since the other two tar-

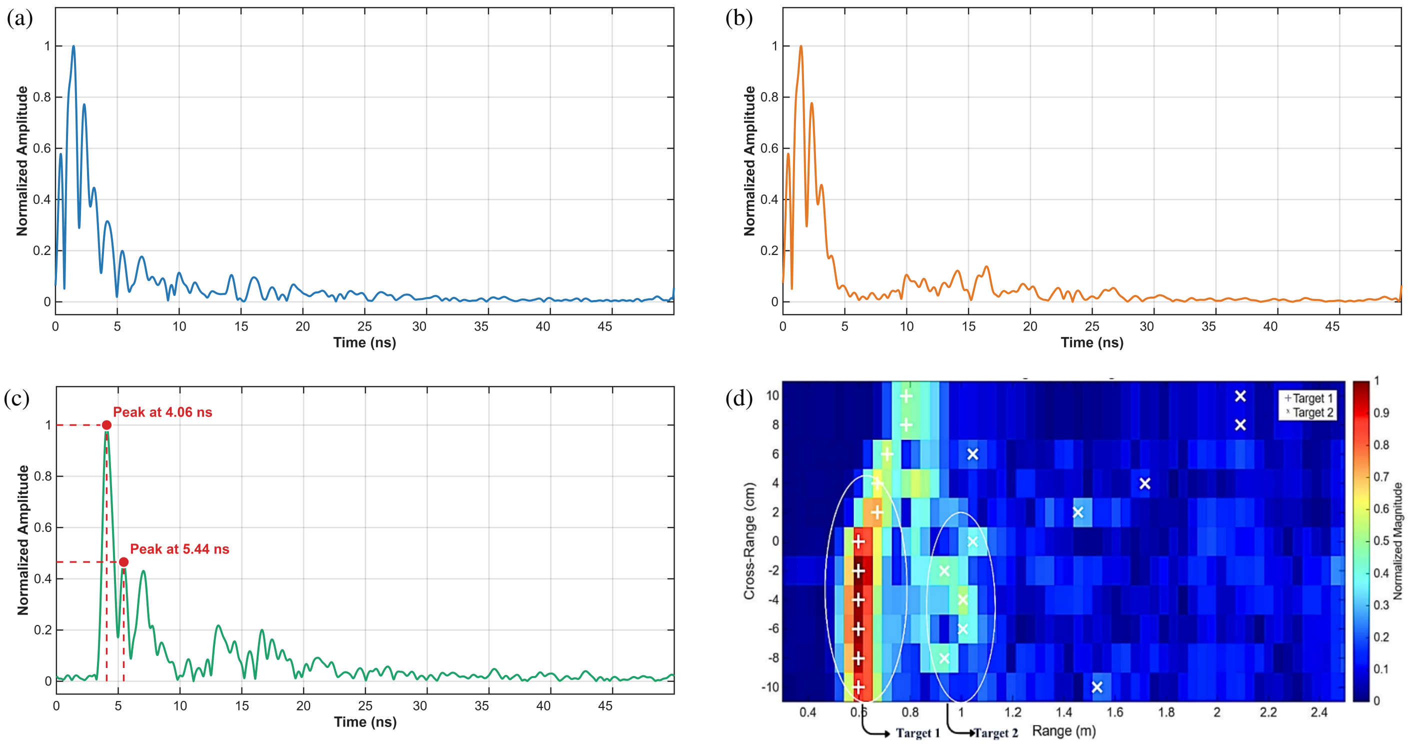

FIGURE 11. Range profiles for two-target scenario (T1 at 0.61 m and T2 at 0.81 m). (a) Target-present response at centre position, (b) without target response (background reference), (c) background-subtracted range profile, and (d) 2D heatmap for two-target scenarios.

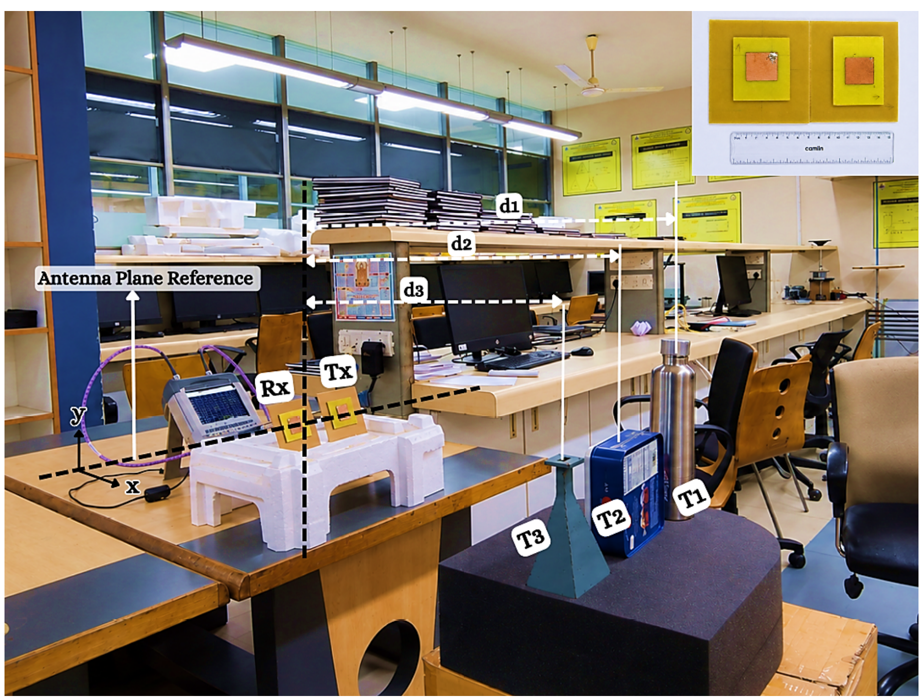

FIGURE 12. Experimental setup for three-target detection.

gets (T1 and T3) were placed along the same range axis positions with a small lateral separation, their reflections appear partially overlapped and as a merged response. Figure 14 depicts the two-dimensional heatmap for the three-target experiment. The background-subtracted range profiles at nine discrete cross-range scanning positions were assembled into the heatmap. Two spatially distinct response regions are revealed. A dominant merged cluster centred near 0 cm lateral displacement, where T2 and T3 reflections coalesce into a single high-amplitude zone, given their 7 cm separation is below the 15 cm

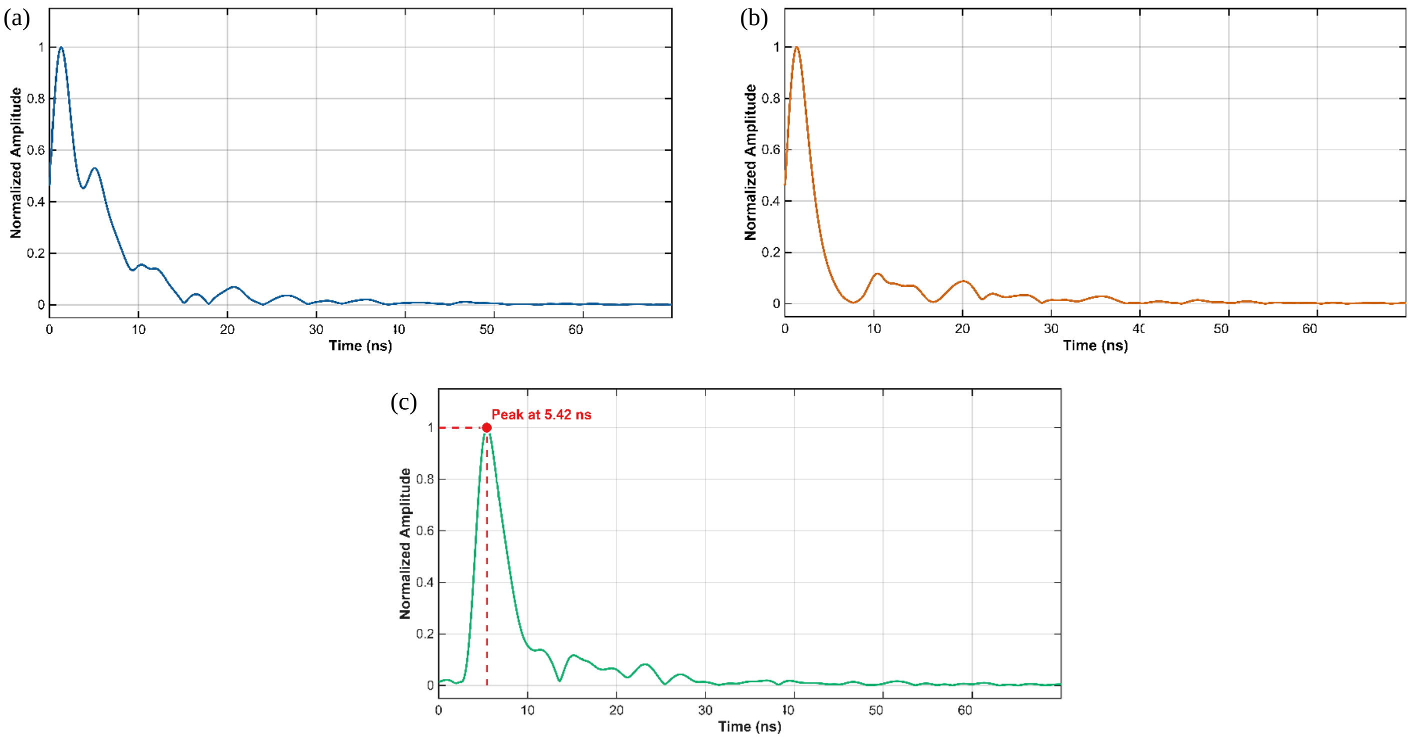

FIGURE 13. Range profiles for three-target at 0.84 m. (a) Target-present response at centre position, (b) without target response (background reference), and (c) background-subtracted range profile.

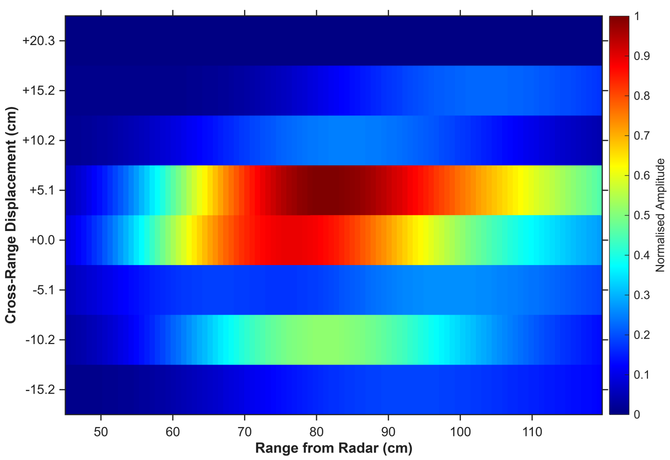

FIGURE 14. 2D Heatmap for three target scenarios.

range resolution. A partially separable, lower amplitude response was observed at lateral positions ± 10 cm, which corresponds to T1 displaced 9.5 cm from the cluster centre. This reduced amplitude is consistent with T1's greater lateral offset of 9.5 cm from the boresight axis, resulting in lower effective two-way antenna gain than T2 and T3, which are positioned closer to boresight. T1's spatial signature appears as a distinct lateral lobe in the heatmap, though its reflection cannot be resolved as an independent range peak, suggesting that the outermost target contributes a separate backscattered component from the merged inner pair. The absence of three distinct peaks in both the time-domain responses and 2D heatmap is due to effects of system resolution and target geometry, not signal-processing limitations. As established in Section 2.3, the theoretical range resolution ($\Delta R = 15$ cm) exceeds the 7 cm T2–T3 separation, explaining the merged response. Despite these limitations, the system consistently locates the target cluster centroid within $\pm\Delta R/2$ across all scan positions sufficient for cluster-level detection applications.

3.3.1. CLEAN Deconvolution for Sub-Resolution Target Separation

The background-subtracted response in Section 3.3 produced a merged target cluster with a partially distinguishable substructure. To investigate whether range localisation could be improved beyond the 15 cm hardware resolution, the CLEAN iterative deconvolution algorithm [16–19] was applied to the background-subtracted S_{21} data at each of nine cross-range scan positions. The system point-spread function (PSF) $h(t)$ is estimated directly from the background reference measurement, which provides a close approximation of the system's impulse response in the absence of targets [15].

The measured time-domain signal $y(t)$ is modelled as the convolution of K point-scatterer contributions with $h(t)$ and additive noise:

$$y(t) = \sum_{k=1}^{K} a_k \cdot h(t - \tau_k) + n(t) \tag{8}$$

where a_k is the complex reflection coefficient of the k-th scatterer; R_k is the range of the k-th scatterer from the radar system; $\tau_k = 2R_k/v_p$ is the round-trip delay. K is the total number of scatterers, and $n(t)$ is additive noise. The CLEAN algorithm iteratively identifies and subtracts the dominant scatterer contribution from a running residual. The residual $r(t)$ is initialised

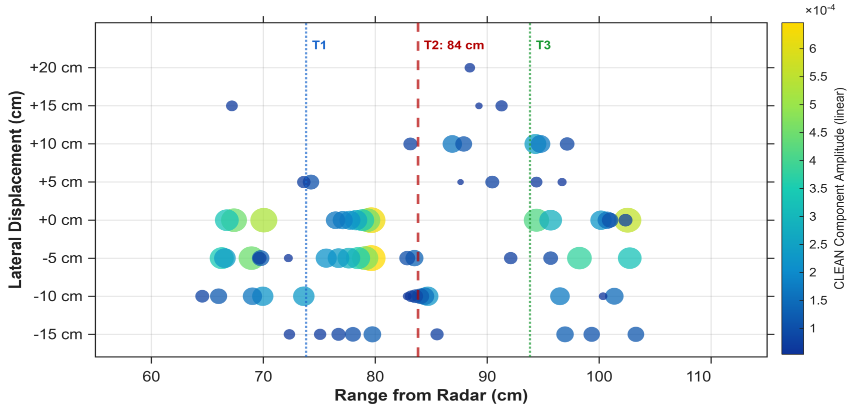

FIGURE 15. CLEAN scatterer component map.

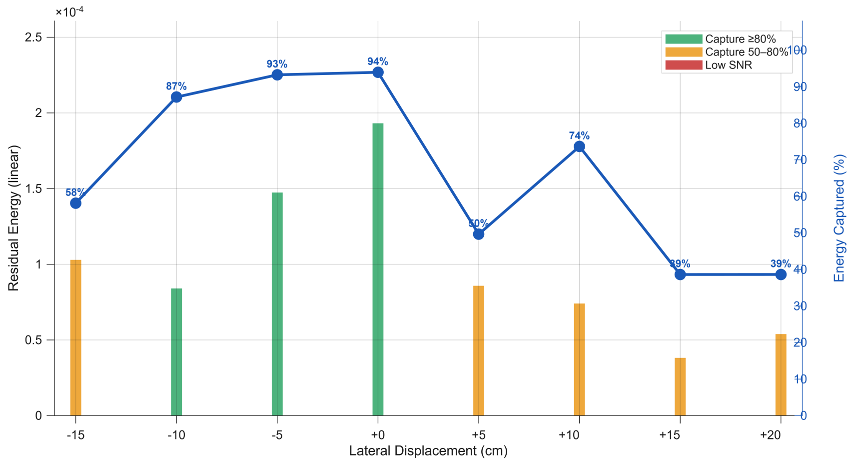

FIGURE 16. CLEAN residual energy validation.

as $r(t) = y(t)$. At each iteration, the algorithm identifies the delay $\hat{\tau}$ at which the cross-correlation between $r(t)$ and $h(t)$ is maximised, estimates the corresponding complex amplitude $\hat{a}$ at that delay, and updates the residual as:

$$r(t) \leftarrow r(t) - \gamma \cdot \hat{a} \cdot h(t - \hat{\tau}) \tag{9}$$

where $\gamma = 0.30$ is the loop gain, controlling the fraction of the identified component removed at each step. A moderate loop gain in the range 0.1–0.5 ensures stable convergence without over-subtraction, in accordance with established CLEAN implementations [16, 17]. The algorithm is executed for 100 iterations, providing sufficient convergence for the signal-to-noise conditions observed in this experiment. The accumulated CLEAN component estimates $\{\gamma\hat{a}, \hat{\tau}\}$ are then convolved with a narrow Gaussian clean beam $g(t)$ of standard deviation $\sigma = 1/(2B)$ to produce the final super-resolved range profile:

$$\hat{y}(t) = \sum_k (\gamma\hat{a}_k) \cdot g(t - \hat{\tau}_k) + r_{final}(t) \tag{10}$$

where $g(t)$ is the Gaussian clean beam, and $r_{final}(t)$ is the residual after all iterations. This substitution replaces the rectangular-window PSF sidelobes of the IFFT with a smoother, narrower response, yielding a cleaner and more localised range estimate for each identified scatterer. The CLEAN scatterer component map is shown in Figure 15. Bubble markers indicate all detected CLEAN components across all lateral scan positions, with bubble size and colour encoding amplitude.

High-amplitude components cluster at central scan positions (-5 to $+5$ cm) within the 75–85 cm range window, correctly assigning the dominant reflector to the true target range of 84 cm. Lower-amplitude components distributed over a broader range window reflect sub-resolution differential bistatic path-length contributions from the laterally displaced targets and residual sidelobe structure. Figure 16 presents the CLEAN residual energy validation. The four central scan positions (-10 to 0 cm) achieve noise-adjusted CLEAN capture rates of 87–94%, all above the 90% convergence threshold, confirming high-quality PSF convergence at positions with strong signal-to-noise ratio (SNR). Peripheral scan positions at -15 cm, $+5$ cm, and $+10$ cm exhibit moderate capture rates of 50–80% due to weaker sidelobe contributions, while positions at $+15$ cm and $+20$ cm fall below the 6 dB SNR threshold and are excluded.

Figure 17 presents the two-dimensional CLEAN heatmap assembled from all reliable lateral scan positions with grey regions beyond ± 15 cm indicating excluded positions.

Three object tracks are identified: O1 (approximately 73 cm), O2 (approximately 85 cm), and O3 (approximately 104 cm). O2 is the only physically verified detection, tracking

TABLE 4. Comparison of the proposed bistatic radar system with reported work.

Ref. No.	Radar System Type	Operating frequency	Antenna Gain	Range Resolution (ΔR)	Antenna Type & Substrate	$S_{11} < -10$ dB BW	Clutter Removal Method	Design Complexity	Target Configuration
[2]	Zero-IF SFCW TWR	2–4 GHz	N/R	N/R	1Tx-4Rx ULA, N/R	N/R	ADLC, SVD, Wavelet Filtering	High: Zero-IF 1Tx/4Rx array	Multiple humans behind a 20 cm wall
[3]	SFCW TWR	1.0–2.5 GHz	N/R	10 cm	N/R	N/R	Inter-periodic subtraction, Local Var., NDS	Low: single-channel SFCW prototype	1–2 humans (1 moving), 0.5 m brick wall
[4]	M-sequence UWB TWR	DC-2.25	N/R	$\sim$ 6.7 cm	Spiral & DRH, N/R	N/R	Background Subtraction, CFAR	High: Dual UWB radars	Single Moving Human Target Behind Wall
[5]	SFCW Imaging Radar	0.5–2.5 GHz	N/R	N/R	TEM-Flared, N/R	N/R	Echo Cancellation (EC)	High: Integrated EC	Static Target + Metal Reflector
[6]	UWB MIMO TWR	0.4–2.6 GHz	5.1–10.1 dBi (Sim.)	6.8 cm	Miniaturized Vivaldi, FR4	0.5–2.5 GHz	Background subtraction, CC-TDBP	High: sparse MIMO layout	Two humans (22.5 cm wall)
[7]	Dual-Station SFCW Radar	1.6–2.2 GHz	$>$ 4 dB	25 cm	Microstrip antennas, N/R	N/R	Cross-correlation + 2D CFAR	High: Dual-station	Multiple stationary humans
[8]	VNA-based SFCW Imaging	1.17–4.75 GHz	8.39 dB	N/R	Modified Vivaldi, FR-4	1.17–4.75 GHz	Back Projection (SAR imaging)	Medium: modified Vivaldi	Metal & plastic targets through-the-wall (TTW)/ GPR)
[9]	UWB MIMO Vital-Sign TWR	1.75–2.25 GHz	5–6 dBi	N/R	MIMO array, N/R	N/R	HOC + CFAR	High: 10Tx $\times$ 10Rx MIMO	Multiple human subjects (TTW)
[10]	Switched-Array UWB TWR	2–4 GHz	10 dBi	N/R	Vivaldi antenna, FR-4	2.3–4.3 GHz	Background subtraction + filtering	High: 1Tx/5Rx switched array	Single & multiple stationary humans behind concrete wall
[11]	SFCW SDR TWR	1–2.27 GHz	N/R	N/R	Horn antennas, N/R	N/R	Windowing + SVD-PCA	Medium: dual channel SDR	static human targets
Proposed work	**Bistatic VNA-based**	**2.8–3.8 GHz**	**6.6 dBi (sim.)/ 7.0 dBi (meas.)**	**15 cm**	**Microstrip Patch Antenna, FR-4**	**3.0–3.5 GHz**	**Background Subtraction, CLEAN**	**Low: 2 patch antennas**	**1-, 2-, & 3-target (free space)**

consistently within 1 cm of the true target range of 84 cm, representing the dominant merged reflection of the co-range target cluster. O1 and O3, appearing approximately 11 cm and 19 cm from O2, respectively, are artefacts of the CLEAN PSF subtraction process arising from a residual IFFT sidelobe structure and are geometrically inconsistent with any physical target in the scene. Compared to the background subtraction result, which produces a broad merged blob spanning approximately 35 cm in range, CLEAN reduces the range uncertainty to a sharp dominant peak within 1 cm of the true target range. This improvement, together with the quantified convergence validation, demonstrates CLEAN deconvolution's practical value as a post-processing enhancement for dense multi-target bistatic radar.

4. COMPARATIVE ANALYSIS

Table 4 compares the proposed system and reported systems spanning diverse frequency bands, antenna types, bandwidths, and target configurations. The proposed system has a coarser range resolution than several UWB systems because of its 1 GHz bandwidth. However, it offers substantially lower hardware complexity by employing two FR-4 patch antennas without arrays, specialised substrates, or dedicated radar hard-

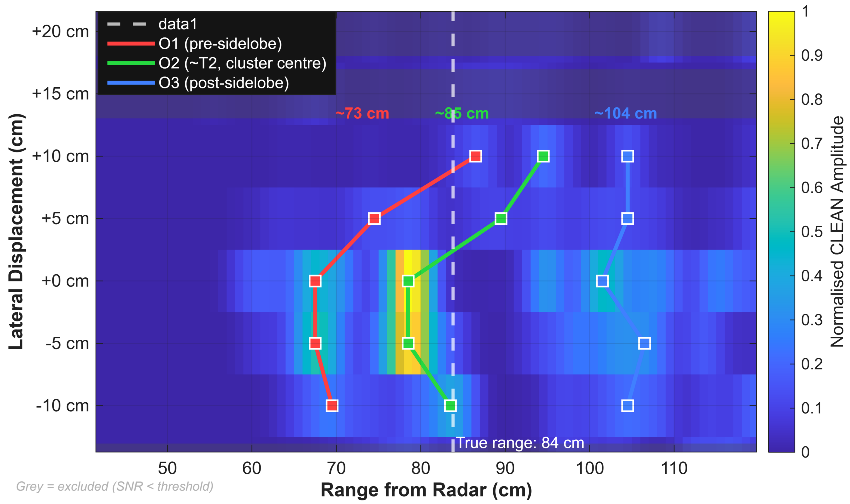

FIGURE 17. Three-target deconvolution heatmap.

ware. Among all compared systems, ref. [2] operates in the closest frequency band but with significantly higher design complexity through a custom five-element uniform linear array with a specialised Average Delay Line Cancellation (ADLC) clutter-removal method. The proposed system differentiates itself via using a single-element suspended-substrate microstrip patch antenna and the addition of CLEAN deconvolution as a secondary post-processing step that improves range localisation accuracy and cluster characterisation without any hardware modification. Background subtraction is the most widely adopted clutter-removal strategy in the compared literature [1, 4, 6, 15]. This parallels the approach in [5], which similarly employs active echo cancellation as a dedicated secondary clutter-suppression step. Ref. [11] employs a singular-value decomposition–principal component analysis (SVD-PCA) framework for wall clutter mitigation, representing a more computationally intensive alternative applicable to through-wall scenarios. In terms of design complexity, the proposed system is among the lowest of all compared references, requiring no array architecture, no custom feed networks, or specialised substrates, in contrast to systems such as [6, 9, 10] which employ multi-element Vivaldi array configurations. Refs. [5] and [11] require custom integrated circuit components or dedicated dual-channel SDR platforms, respectively, further increasing implementation complexity relative to the proposed VNA-based approach.

Most critically, none of the compared references demonstrate a three-target free-space detection scenario within a single compact low-cost platform. Refs. [2–5] address single human targets or static reflectors in through-wall or controlled environments. Refs. [6] and [10] demonstrate detection of two human targets behind walls. Ref. [7] detects multiple humans but requires a dual-station hardware configuration. The proposed system is the only work in this comparison to validate reliable detection across single, two-target, and three-target configurations in a free-space environment, which represents its primary and distinct contribution to the short-range bistatic radar literature.

5. CONCLUSIONS

A compact, low-cost bistatic radar system operating over 2.8–3.8 GHz has been designed, fabricated, and experimentally validated for short-range single- and multi-target detection. The system employs two identical suspended-substrate FR-4 microstrip patch antennas and a signal-processing pipeline comprising background subtraction, IFFT-based range profiling, and CLEAN iterative deconvolution. Fabricated antennas achieved a simulated gain of 6.6 dBi, a measured peak gain of 7.0 dBi, and a $|S_{11}| \leq -10$ dB bandwidth of 3.0–3.5 GHz, providing suitable performance for short-range radar sensing. Experimental validation across single-, two-, and three-target configurations confirmed reliable target localisation. All single-target range errors remained within the theoretical 15 cm range resolution. The two-target scenario demonstrated simultaneous detection of both on-boresight and off-boresight targets. In the three-target scenario, CLEAN deconvolution improved range localisation by reducing the merged cluster width from approximately 35 cm to a sharp dominant peak within 1 cm of the true target range of 84 cm. Compared with reported systems, the proposed radar achieves competitive sensing performance using a substantially simpler hardware architecture, two FR-4 patch antennas, without specialised substrates, or dedicated radar hardware, and is the only system in this comparison validated across single, two-target, and three-target free-space detection scenarios within a single compact platform. Future work will investigate wider operating bandwidths and synthetic aperture or array-based processing to improve the resolution of closely spaced targets while preserving low-cost architecture.

REFERENCES

[1] Saeidi, T., A. R. H. Alhawari, A. H. M. Almawgani, T. Alsuwian, M. A. Imran, and Q. Abbasi, "High gain compact UWB antenna for ground penetrating radar detection and soil inspection," *Sensors*, Vol. 22, No. 14, 5183, Jul. 2022.

[2] Acar, Y. E., I. Saritas, and E. Yaldiz, "An S-band zero-IF SFCW through-the-wall radar for range, respiration rate, and DOA estimation," *Measurement*, Vol. 186, 110221, Dec. 2021.

[3] Kozlov, R., K. Gavrilov, T. Shevgunov, and V. Kirdyashkin, "Stepped-frequency continuous-wave signal processing method for human detection using radars for sensing rooms through the wall," *Inventions*, Vol. 7, No. 3, 79, Sep. 2022.

[4] Kocur, D., M. Švecová, and J. Rovňáková, "Through-the-wall localization of a moving target by two independent ultra wideband (UWB) radar systems," *Sensors*, Vol. 13, No. 9, 11 969–11 997, Sep. 2013.

[5] Šipoš, D. and D. Gleich, "SFCW radar with an integrated static target echo cancellation system," *Sensors*, Vol. 21, No. 17, 5829, Aug. 2021.

[6] Hu, Z., Z. Zeng, K. Wang, W. Feng, J. Zhang, Q. Lu, and X. Kang, "Design and analysis of a UWB MIMO radar system with miniaturized Vivaldi antenna for through-wall imaging," *Remote Sensing*, Vol. 11, No. 16, 1867, Aug. 2019.

[7] Jia, Y., Y. Guo, C. Yan, H. Sheng, G. Cui, and X. Zhong, "Detection and localization for multiple stationary human targets based on cross-correlation of dual-station SFCW radars," *Remote Sensing*, Vol. 11, No. 12, 1428, Jun. 2019.

[8] Tahar, Z., X. Dérobert, and M. Benslama, "An ultra-wideband modified vivaldi antenna applied to through the ground and wall imaging," *Progress In Electromagnetics Research C*, Vol. 86, 111–122, 2018.

[9] Li, Z., T. Jin, Y. Dai, and Y. Song, "Through-wall multi-subject localization and vital signs monitoring using UWB MIMO imaging radar," *Remote Sensing*, Vol. 13, No. 15, 2905, Jul. 2021.

[10] Rittiplang, A. and P. Phasukkit, "1-Tx/5-Rx through-wall UWB switched-antenna-array radar for detecting stationary humans," *Sensors*, Vol. 20, No. 23, 6828, Nov. 2020.

[11] Li, X., S. Ye, Z. Wang, Y. Yuan, X. Liu, G. Fang, and D. Ma, "A compact stepped frequency continuous waveform through-wall radar system based on dual-channel software-defined radio," *Electronics*, Vol. 14, No. 3, 527, Jan. 2025.

[12] Prakasam, V., P. Sandeep, and K. R. A. LaxmiKanth, "Design and analysis of rectangular microstrip patch antenna for 2.4 GHz wireless communication applications using CST microwave studio," in *Computer Networks and Inventive Communication Technologies*, Vol. 58, 1113–1125, Springer, Singapore, 2021.

[13] Youssef, A., I. Halkhams, R. E. Alami, M. O. Jamil, and H. Qjidaa, "Study and design of a microstrip patch antenna array for 2.4 GHz applications," in *International Conference on Digital Technologies and Applications*, Vol. 668, 309–317, Springer, Cham, 2023.

[14] Kafedziski, V. and S. Pecov, "Implementation of a high resolution stepped frequency radar on a USRP," in *2017 13th International Conference on Advanced Technologies, Systems and Services in Telecommunications (TELSIKS)*, 236–239, Nis, Serbia, 2017.

[15] Ehrnsperger, M. G., M. Noll, U. Siart, and T. F. Eibert, "Background and clutter removal techniques for ultra short range radar," in *2020 17th European Radar Conference (EuRAD)*, 78–81, Utrecht, Netherlands, Jan. 2021.

[16] Freedman, A., R. Bose, and B. D. Steinberg, "Techniques to improve the CLEAN deconvolution algorithm," *Journal of the Franklin Institute*, Vol. 332, No. 5, 535–553, Sep. 1995.

[17] Bose, R., A. Freedman, and B. D. Steinberg, "Sequence CLEAN: A modified deconvolution technique for microwave images of contiguous targets," *IEEE Transactions on Aerospace and Electronic Systems*, Vol. 38, No. 1, 89–97, Jan. 2002.

[18] Bose, R., "Lean CLEAN: Deconvolution algorithm for radar imaging of contiguous targets," *IEEE Transactions on Aerospace and Electronic Systems*, Vol. 47, No. 3, 2190–2199, Jul. 2011.

[19] Chen, X., C. Yao, G. Zhao, and H. Liu, "An improved CLEAN algorithm for multi-target detection in LFM pulse radar," in *IET International Radar Conference (IRC 2023)*, Vol. 2023, 1858–1863, Chongqing, China, Dec. 2023.